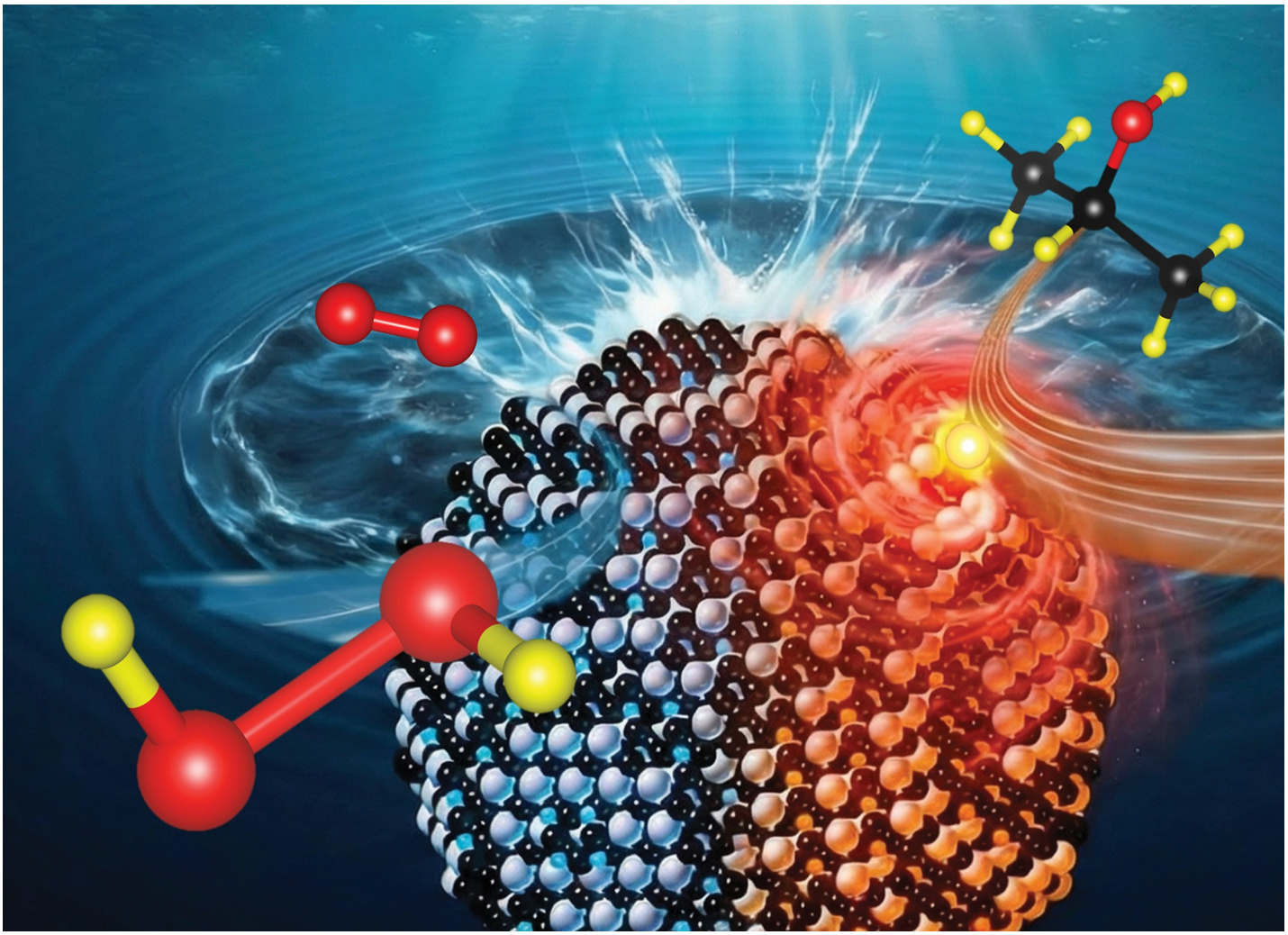

Showcasing research from Professor Habazaki's laboratory, Faculty of Engineering, Hokkaido University, Japan.

Single-atom rhodium on $BaTiO_3$ for enhanced piezocatalytic H_2O_2 production *via* promotion of oxidative ability

Atomically dispersed Rh^{3+} single atoms were anchored on tetragonal $BaTiO_3$ as a surface cocatalyst to enhance piezocatalytic H_2O_2 production by selectively accelerating isopropanol oxidation *via* piezo-generated positive charges.

Image reproduced by permission of Sho Kitano from *Phys. Chem. Chem. Phys.*, 2026, **28**, 6190.
Image created using Adobe Firefly.

As featured in:

See Sho Kitano, Hiroki Habazaki *et al.*, *Phys. Chem. Chem. Phys.*, 2026, **28**, 6190.

PCCP

PAPER

View Article Online
View Journal | View Issue

Cite this: *Phys. Chem. Chem. Phys.*, 2026, **28**, 6190

Single-atom rhodium on $BaTiO_3$ for enhanced piezocatalytic H_2O_2 production *via* promotion of oxidative ability

Sho Kitano, *[a] Yuta Nagasaka,[b] Shunya Yoshida,[b] Mana Iwai,[a] Koji Fushimi[a] and Hiroki Habazaki *[a]

Received 23rd December 2025,
Accepted 17th January 2026

DOI: 10.1039/d5cp04993h

rsc.li/pccp

Piezocatalysis is a promising method for generating green hydrogen peroxide (H_2O_2), however, improving the surface charge transfer kinetics remains challenging. In this study, we develop tetragonal barium titanate (BTO) nanoparticles modified with surface-anchored rhodium single-atom (RhSA) cocatalysts. Detailed structural characterization confirmed that the Rh species are atomically dispersed as Rh^{3+} coordinated with surface oxygen of BTO without forming clusters or being incorporated into the BTO lattice. Piezoresponse force microscopy revealed that RhSA does not affect the intrinsic piezoelectric polarization of the BTO. However, the BTO–RhSA catalyst produced 1.5 times more H_2O_2 than pristine BTO did under ultrasonic excitation. Mechanistic studies using (piezo)electrochemical measurements demonstrated that unlike conventional noble metal cocatalysts, which typically enhance the reduction kinetics, the RhSA sites on BTO do not promote the oxygen reduction reaction (ORR). Instead, they significantly accelerate the oxidation of isopropanol as a sacrificial reagent by efficiently utilizing the piezo-generated positive charges. This work establishes a surface-engineering strategy in which isolated atomic sites selectively boost positive charge-driven reactions, enabling the independent control of reduction and oxidation pathways and providing new design principles for high-performance piezocatalytic systems.

1. Introduction

Hydrogen peroxide (H_2O_2) is an environmentally friendly oxidizing agent widely used in chemical synthesis, disinfection, environmental remediation, and emerging energy-related applications.[1] Despite the continuously increasing global demand for H_2O_2, its industrial-scale production relies almost entirely on the anthraquinone auto-oxidation process, which is energy-intensive and environmentally harmful. Therefore, the development of sustainable H_2O_2 production technologies has become a major research challenge in recent years.[2–5] Among various alternative technologies, piezocatalytic reactions have garnered significant attention in recent years.[6–8] Piezocatalytic reactions are driven by the inherent piezoelectric properties of non-centrosymmetric materials, such as $BaTiO_3$,[9] ZnO,[10] $BiFeO_3$,[11] $KNbO_3$,[12] MoS_2,[13] and PVDF-based polymers.[14] When mechanically deformed, these materials generate an internal electric field that spatially separates the charge carriers and forms an interfacial potential gradient capable of driving redox reactions. Over the past decade, piezocatalysts have been successfully applied to various reactions such as water disinfection,[15] nitrogen fixation[16] and CO_2 reduction.[17] In particular, piezocatalytic H_2O_2 production provides an eco-friendly pathway that uses only oxygen and water as reactants.[8] However, the efficiency of piezocatalysts remains significantly lower than that of other green synthetic routes including photocatalysts and electrocatalysts. This highlights the need for rational strategies to enhance their piezoelectric catalytic activity.

Several materials engineering approaches have been proposed to address this challenge. Controlling the material morphology enables greater deformation under mechanical stimulation, which significantly influences its piezocatalytic performance. Piezocatalysts fabricated in one-dimensional nanowire or two-dimensional nanosheet morphologies have been reported to exhibit high activities.[18,19] Defect engineering improves charge mobility and promotes radical generation.[20–22] Recent reports indicate that vacancies enhance piezoelectricity and facilitate charge carrier separation.[20,22] Interface heterostructure designs, such as the construction of Schottky barriers at oxide–nitride and oxide–sulfide interfaces, enhance charge separation under mechanical excitation.[23–25] Composites containing MoS_2, ZnO, or g-C_3N_4 demonstrated improved charge transfer and retention.

Although these efforts have contributed to improving the piezocatalytic activity, achieving a sufficient level of performance

[a] *Division of Applied Chemistry, Faculty of Engineering, Hokkaido University, Sapporo, Hokkaido 060-8628, Japan. E-mail: skitano@eng.hokudai.ac.jp*
[b] *Graduate School of Chemical Sciences and Engineering, Hokkaido University, Sapporo, Hokkaido 060-8628, Japan*

remains challenging. These approaches primarily focus on enhancing the intrinsic piezoelectric properties or promoting charge migration within the bulk of piezocatalytic materials. While such strategies effectively improve the internal processes associated with piezocatalysis, another important approach to achieving high performance is boosting surface catalytic reactions driven by piezo-generated charges.

Loading metal nanoparticle co-catalysts is a highly effective strategy for enhancing reactions using piezoelectric charges at the surface.[26,27] Efficient interfacial charge transfer pathways can be created by loading co-catalysts onto piezocatalysts, facilitating charge separation between the two, and enhancing oxidation or reduction reactions at the co-catalyst sites. Lin *et al.* reported that Ag nanoparticles supported on $BaTiO_3$ promoted charge separation by acting as electron traps, thereby improving the piezocatalytic activity.[28] In addition to Ag, other metal nanoparticle cocatalysts, such as Pt,[29] Au,[30] and Pd,[31] have been employed in piezocatalytic systems, achieving significant enhancements in various reactions. These findings indicate that strategies that accelerate surface reaction kinetics are critically important for developing highly active piezocatalytic systems, in addition to improving bulk properties. However, compared with studies on other strategies for enhancing the activity of piezocatalysts, research on cocatalysts remains limited. Therefore, exploring more diverse and efficient co-catalysts will improve the performance of piezocatalysts and expand their potential applications.

Single-atom engineering is expected to be a breakthrough in enhancing piezocatalytic activity. In recent years, single-atom catalysts, in which catalytically active metal species are dispersed as isolated atomic sites on solid supports, have emerged as a new frontier in heterogeneous catalysis.[32,33] Single atoms exhibit the highest atomic utilization efficiency compared with that of nanoparticle catalysts. Furthermore, metal centers dispersed at the atomic level act as unique active sites with distinctive coordination environments that are not achievable in nanoparticle-based co-catalysts. For example, surface-loaded single atoms have been reported to promote specific redox processes as co-catalysts in photocatalyst research.[34,35] In particular, Rh single atoms supported on TiO_2 have been reported to accelerate alcohol oxidation and oxygen reduction in photocatalysis.[36–39] Single atoms have also been introduced into piezocatalytic systems, demonstrating enhanced activity.[40–42] However, single atoms were incorporated into the bulk lattice of the piezoelectric materials, primarily contributing to improvements in the internal material properties. To our knowledge, no study has examined surface-loaded single atoms as co-catalysts specifically designed to accelerate surface reactions in piezocatalysis. The potential of surface single-atom sites to accelerate oxidation or reduction reactions will pioneer new design approaches for next-generation piezoelectric catalytic systems.

In this study, we examine a novel strategy for enhancing piezocatalytic H_2O_2 production by modifying tetragonal $BaTiO_3$ (BTO) nanoparticles with surface-anchored Rh atoms (RhSA). The resulting RhSA-loaded BTO (BTO–RhSA) catalyst exhibits a 1.5-fold increase in H_2O_2 production compared with that of the pristine BTO. Detailed mechanistic analyses reveal that this enhancement stems not from improved oxygen reduction activity, but from the promotion of the oxidation reaction of the sacrificial substrate isopropanol. These findings demonstrate for the first time that single-atom surface loading can selectively accelerate the oxidation half-reaction in piezocatalysis, overcoming a critical rate-limiting step. This study presents a novel design principle for high-performance piezocatalysts and highlights the decisive importance of oxidation kinetics in piezocatalytic systems.

2. Experimental

2.1. Synthesis of BTO nanoparticles

BTO nanoparticles were synthesized *via* a two-step hydrothermal process based on a previously reported method.[43] In the first step, $K_{0.8}Li_{0.27}Ti_{1.73}O_4$ (KLTO) precursor was prepared. $LiOH{\cdot}H_2O$ (0.36 g, FUJIFILM Wako), KOH (3.06 g, Kojundo Chemical), TiO_2 powder (4.14 g, JRC-TIO-9, Furukawa Co.), and ethanol (25 mL, Kanto Chemical) were added to a 50 mL Teflon-lined autoclave and mixed thoroughly. The autoclave was then heated at 150 °C for 24 h to obtain the KLTO. The resulting solid was collected and proton-exchanged by immersing it in 1 M HNO_3 (Kanto Chemical) for 24 h to yield $H_2Ti_4O_9$ (HTO).

In the second hydrothermal step, BTO was formed by the reaction of HTO with $Ba(OH)_2$. A 90 mM $Ba(OH)_2$ solution (15 mL, prepared using a 1 : 4 water/ethanol mixture) and HTO (0.147 g) were added to a 50 mL Teflon autoclave. The mixture was heated at 200 °C for 4.5 h. After cooling to room temperature, the product was washed repeatedly with 0.1 M acetic acid (Kanto Chemical) followed by deionized water and finally collected by centrifugation. The obtained powder was dried and used as the BTO catalyst.

2.2. Loading of RhSA on BTO nanoparticles

The surface loading of RhSA was conducted according to a modified literature procedure.[44] BTO powder (80 mg) was dispersed in deionized water (50 mL). An aqueous $RhCl_3$ solution (Kanto Chemical) of the desired concentration was added to the suspension under constant stirring. The suspension was then heated at 95 °C in an oil bath for 1 h under continuous stirring to load RhSA onto the BTO surface. After the reaction, the suspension was cooled, centrifuged, and washed thoroughly with water to remove the chloride ions. All samples were dried and stored before use. The BTO–RhSA samples were prepared with Rh loadings of 0.2, 1.0, and 2.0 wt% relative to BTO. The actual Rh loading was confirmed by inductively coupled plasma optical emission spectroscopy analysis (ICP-OES, iCAP 7400, Thermo Fisher Scientific) of the supernatant after the loading process. No detectable Rh species remained in the solution, indicating that the introduced Rh precursor was quantitatively loaded onto the BTO surface. Therefore, the nominal Rh loadings represent the actual Rh contents in the synthesized catalysts.

2.3. Evaluation of piezocatalytic activity

Piezocatalytic H_2O_2 production was evaluated using an ultrasonic-vibration system (VS-150, AS ONE Corp.). For each

experiment, 5 mg of the catalyst was dispersed in a mixed solvent consisting of 2.5 mL of deionized water and 2.5 mL of isopropanol (Kanto Chemical) in a test tube. After purging the suspension with O_2 to ensure oxygen saturation, the test tube was sealed with a rubber stopper and fixed at a constant position inside an ultrasonic bath. Ultrasonic irradiation was performed at 50 kHz and 150 W, while maintaining the bath temperature at 35 °C using a circulating thermostat. Every 15 min, 0.2 mL aliquots of the reaction mixture were withdrawn for H_2O_2 analysis, and an equal volume (0.2 mL) of fresh mixed solvent was added to maintain a constant reaction volume. For H_2O_2 quantification, each aliquot was diluted with 4.8 mL of deionized water and centrifuged to remove the catalyst particles. The supernatant was then mixed with a colorimetric H_2O_2 indicator reagent (PackTest, Kyoritsu Chemical Research Co.), and the absorbance was measured at 539 nm using a UV–Vis spectrophotometer (V-550, JASCO Corp.). H_2O_2 concentrations were determined from a calibration line generated using standard H_2O_2 solutions (Kanto Chemical).

2.4. Characterization

A scanning electron microscope (SEM, ZEISS Sigma 500) operating at an acceleration voltage of 1.5 kV was used to examine powder morphology. The powders were directly mounted on carbon tape and imaged after evacuation. Transmission electron microscopy (TEM, JEOL JEM-2100) at 200 kV was used for detailed structural observations. The TEM specimens were prepared by dispersing the samples in ethanol, dropping the suspension onto microgrids, and drying under vacuum. High-resolution elemental mapping was carried out using scanning transmission electron microscopy (STEM, JEOL JEM-ARM200F) operated at 200 kV. The STEM specimens were prepared using the same manner as the TEM samples. Crystalline phases were identified by X-ray diffraction (XRD, Rigaku SmartLab SE) using a multipurpose diffractometer equipped with Cu-Kα radiation (λ = 0.15418 nm) operated at 40 kV and 30 mA. X-ray photoelectron spectroscopy (XPS) was conducted using a JPS-9200 spectrometer (JEOL) equipped with Mg-Kα radiation ($h\nu$ = 1253.6 eV). The powder samples were pressed onto indium foil using aluminum foil to ensure complete coverage. All the spectra were calibrated against the C 1s peak at 285.0 eV. Piezoresponse force microscopy (PFM) measurements were performed using an atomic force microscope (AFM, Bruker Dimension Icon) with an SCM-PIT-V2 probe with PtIr-coating with a resonance frequency of 75 kHz and a spring constant of 3 N m^{-1}. X-ray absorption fine structure (XAFS) spectra were recorded at the BL07 of the SAGA Light Source. The storage ring operated at 1.4 GeV, and Si (220) single crystals were used to obtain monochromatic X-ray beams at the Rh K-edge. The catalysts were measured in fluorescence mode using an ion chamber/solid-state detector (SDD), whereas the references were measured in transmission mode using ion chambers. The XANES and EXAFS spectra were processed using Athena software.

2.5. Electrochemical and piezo-electrochemical measurements

Electrochemical oxygen reduction reaction (ORR) measurements were performed using a rotating disk electrode (RDE) setup. Catalyst inks were prepared by dispersing BTO or BTO–RhSA powders into acetone to obtain a concentration of 1 mg cm^{-3}, followed by drop-casting onto a glassy carbon (GC) electrode at a loading of 0.5 mg cm^{-2}. A three-electrode configuration was used with a GC working electrode, Ag/AgCl reference electrode, and Pt counter electrode. The electrolyte was a 0.1 M phosphate buffer solution (pH 6.8). Linear sweep voltammetry (LSV) was performed from 1.1 to −0.02 V *vs.* RHE at a scan rate of 10 mV s^{-1} under continuous O_2 bubbling to evaluate the ORR activity. All electrochemical measurements were performed at room temperature.

The oxidation ability of the catalysts was further examined using piezoelectrochemical measurements. Catalyst inks with a concentration of 1 mg cm^{-3} were prepared by dispersing the powders in acetone and subsequently coated onto 2 × 2 cm fluorine-doped tin oxide (FTO) substrates, followed by drying at room temperature to obtain electrodes with a catalyst loading of 0.2 mg cm^{-2}. The electrode was placed in a three-electrode cell with an Ag/AgCl reference electrode and Pt counter electrode. The electrolyte was a 0.1 M Na_2SO_4 aqueous solution containing 0.01 M isopropanol. The cell was placed inside the bath of an ultrasonic irradiation system, and chronoamperometric measurements were conducted at an applied bias of 1.0 V *vs.* the RHE. During the experiment, ultrasonic irradiation at 50 kHz and 150 W was switched on and off at predetermined intervals, and the resulting changes in current density were recorded to evaluate the influence of piezoelectric polarization on the oxidative reaction processes.

3. Results and discussion

3.1. Structural and morphological characterization

XRD analysis revealed that the obtained BTO nanoparticles exhibited sharp and well-defined diffraction peaks, indicating their high crystallinity (Fig. 1a). All the diffraction peaks were indexed to the tetragonal perovskite phase of $BaTiO_3$, with no detectable secondary phases, confirming the phase purity of the product.[45] Morphological characterization by SEM and TEM showed that the synthesized powders consisted of irregularly shaped, nearly spherical nanoparticles with diameters of several tens of nanometers (Fig. 1b and c). High-resolution bright-field STEM (BF-STEM) imaging revealed distinct lattice fringes with an interplanar spacing of approximately 0.396 nm. This corresponds to the (100) plane of tetragonal BTO (Fig. 1d). These structural and morphological analyses confirmed that the hydrothermal synthesis yielded highly crystalline tetragonal BTO nanoparticles with a well-defined lattice structure suitable for subsequent piezocatalytic studies. The crystalline structure of BTO–RhSA was analyzed using XRD. The diffraction pattern of BTO–RhSA was similar to that of pristine BTO, displaying characteristic reflections of the tetragonal structure without any detectable peak shifts or broadening (Fig. 1a). No additional reflections associated with metallic Rh, Rh_2O_3, or other Rh-containing crystalline phases were observed. These results suggest that the introduction of Rh species does not influence

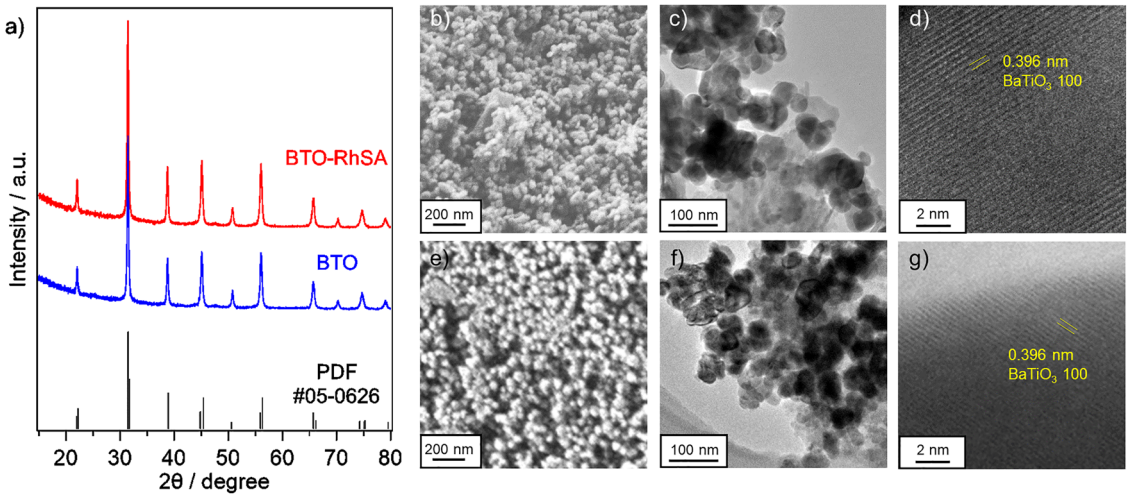

Fig. 1 XRD patterns of (a) the pristine BTO and BTO–RhSA. SEM micrographs of (b) the pristine BTO and (e) BTO–RhSA. (c) and (f) Low and (d) and (g) high-resolution TEM micrographs of (c) and (d) the pristine BTO and (f) and (g) BTO–RhSA.

the bulk crystal structure of BTO and that Rh species do not form crystalline nanoparticles or rhodium oxide phases. This behavior is consistent with previous reports on RhSA loading onto TiO_2 photocatalysts.[46] The particle morphology and size of BTO–RhSA remained unchanged compared with those of pristine BTO, exhibiting irregular, nearly spherical nanoparticles with diameters of several tens of nanometers (Fig. 1e and f). High-magnification BF-STEM images revealed that no particulate Rh domains existed, indicating the absence of metallic Rh clusters and amorphous Rh oxide aggregates in the BTO–RhSA. The lattice fringe spacing corresponding to the (100) plane of tetragonal BTO observed in BTO–RhSA was 0.396 nm, identical to the lattice plane spacing of pristine BTO (Fig. 1g). The absence of detectable Rh-containing nanoparticles in both the diffraction patterns and TEM observations strongly suggests that Rh exists in a highly dispersed atomic state.

High-angle annular dark-field STEM (HAADF-STEM) observation and EDX elemental mapping provided more definitive evidence of the Rh dispersion state. As shown in Fig. 2a–c, the Ba and Ti signals overlapped with the morphology of individual BTO nanoparticles. Notably, Rh signals were uniformly observed over the BTO particles without localized high-intensity spots corresponding to Rh-containing clusters or nanoparticles (Fig. 2d). Given that HAADF-STEM exhibits high sensitivity to atomic number contrast, the absence of detectable Rh-containing clusters suggests that Rh is stabilized as isolated atomic species on the BTO surface. XRD, STEM, and EDX analyses clearly demonstrated that Rh did not incorporate into the BTO lattice or form any Rh-containing nanoparticles. Instead, Rh was uniformly dispersed at isolated atomic sites on the BTO surface.

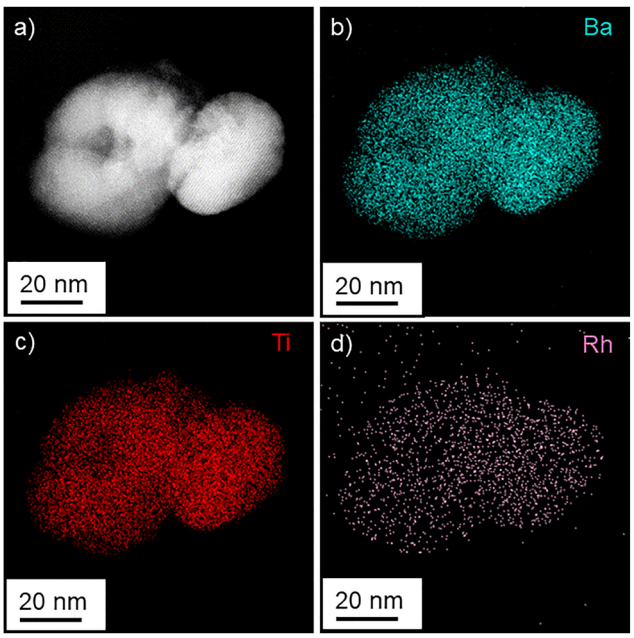

Fig. 2 (a) HAADF-STEM image of BTO–RhSA and corresponding EDX elemental mappings for (b) Ba, (c) Ti, and (d) Rh.

3.2. Chemical and coordination state analysis

X-ray photoelectron spectroscopy (XPS) analyses were conducted on both pristine BTO and BTO–RhSA to elucidate the chemical states of the constituent elements (Fig. 3). The Ti 2p spectrum of BTO exhibited two well-defined peaks at 458.0 eV (Ti $2p_{3/2}$) and 463.8 eV (Ti $2p_{1/2}$), which are characteristic of Ti^{4+} species in tetragonal BTO. Likewise, the Ba 3d spectrum displayed peaks at approximately 778.0 eV (Ba $3d_{5/2}$) and 793.4 eV (Ba $3d_{3/2}$), confirming the presence of Ba in the Ba^{2+} oxidation state. These values are consistent with the previously reported reference spectra for high-purity BTO.[47] The Ti 2p and Ba 3d spectra of BTO–RhSA showed peak energy positions similar to those of pristine BTO, indicating that the introduction of RhSA did not change the electronic states of BTO. This observation coincides with structural analyses showing that Rh did not substitute into the BTO lattice or induce lattice distortion. The Rh 3d spectrum of BTO–RhSA exhibited a distinct peak at

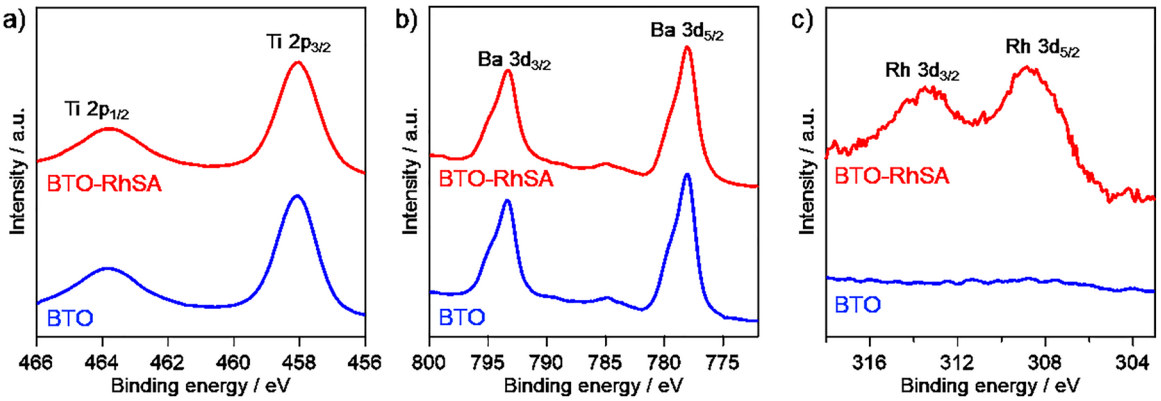

Fig. 3 XPS spectra for (a) Ti 2p, (b) Ba 3d and (c) Rh 3d of the pristine BTO and BTO–RhSA.

308.6 eV, corresponding to the Rh $3d_{5/2}$ level. This binding energy closely matches the reported value for Rh^{3+} species in Rh_2O_3 (308.8 eV) and is significantly higher than that of metallic Rh (307.6 eV). This result indicates that Rh does not exist in metallic states. Thus, the Rh species introduced onto the BTO surface were predominantly in the Rh^{3+} oxidation state. This oxidation state assignment is consistent with previous reports on Rh single atoms stabilized on TiO_2 supports.[38,44] The XPS analysis also confirmed the absence of detectable impurity elements, including chlorine, indicating that residual precursor-derived species were effectively removed during the synthesis and washing processes.

XAFS measurements were conducted to elucidate the oxidation state and coordination environment of the Rh species anchored on BTO. Fig. 4a compares the Rh K-edge X-ray absorption near-edge structure (XANES) spectra of the Rh foil, Rh_2O_3, and BTO–RhSA samples. The absorption edge of the XANES spectrum for BTO–RhSA (23 236.9 eV) is similar to that for Rh_2O_3 (23 237.0 eV) and is clearly distinct from that of metallic Rh (23 234.0 eV), indicating that Rh exists predominantly in the +3 oxidation state. This oxidation state assignment is consistent with the XPS results. Fig. 4b shows the k^3-weighted Rh K-edge Fourier-transformed extended XAFS (EXAFS) spectra for Rh foil, Rh_2O_3, and BTO–RhSA. The Rh_2O_3 reference exhibits three major peaks at approximately 1.60, 2.64, and 3.34 Å, corresponding respectively to the Rh–O first shell and multiple Rh–Rh coordination shells. In contrast, the BTO–RhSA sample exhibited only a single prominent peak at 1.60 Å, attributable to Rh–O scattering. No higher-shell peaks corresponding to Rh–Rh coordination were detected, indicating the absence of Rh–Rh interactions typically observed for nanoparticles or clusters. These results strongly support the atomic dispersion of Rh as isolated Rh^{3+} sites on the BTO surface. Considering that the chloride anions were thoroughly removed through repeated washing steps during preparation, the charge compensation of Rh^{3+} is achieved through coordination with surface oxygen species and water-derived hydroxyl groups. The isolated Rh^{3+} species likely adopt a geometry coordinated by multiple oxygen-containing ligands, including deprotonated surface hydroxyl groups, terminal oxide ions, hydroxide anions, and water molecules (Fig. 4c). Such coordination structures provide the necessary charge balance and resemble the structural motifs reported for RhSA complexes on oxide supports.[38] These surface oxygen-containing ligands not only stabilize the positively charged Rh centers but also prevent aggregation, contributing to the high Rh dispersion. Furthermore, the BTO–RhSA samples with various Rh loadings displayed comparable XANES spectra (Fig. S1a). EXAFS spectra showed a single Rh–O coordination peak near 1.60 Å and no Rh-Rh coordination, confirming that Rh remained atomically dispersed regardless of the RhSA amount (Fig. S1b). The Rh loadings based on the formula unit were calculated as follows.

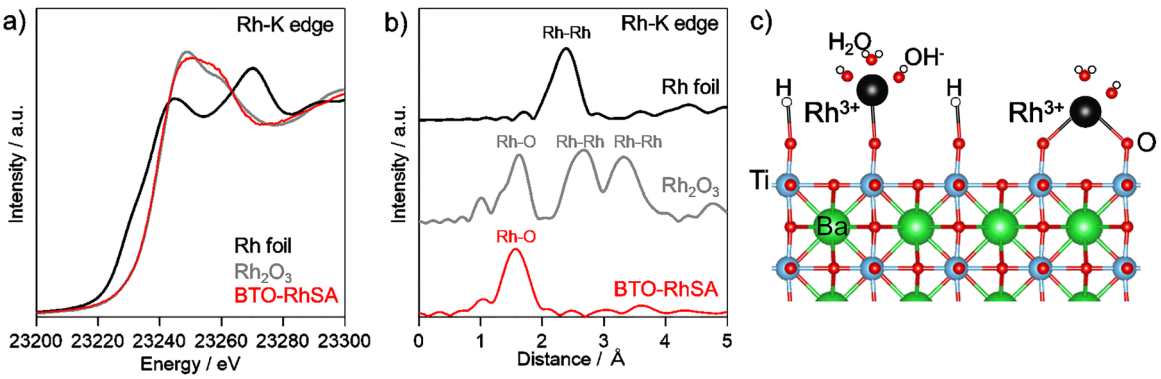

Fig. 4 (a) Rh K-edge XANES spectra and (b) Fourier transforms (FT) of k_3-weighted Rh-K edge EXAFS spectra of the BTO–RhSA, Rh foil and Rh_2O_3. (c) Illustration of RhSA anchored on the surface of BTO.

The 0.2, 1.0, and 2.0 wt% Rh loadings correspond to approximately 0.0046, 0.023, and 0.046 Rh atoms per $BaTiO_3$ formula unit, respectively (*i.e.*, approximately one Rh atom per 217, 43, and 22 $BaTiO_3$ formula units, respectively). These values quantitatively demonstrate that Rh atoms exist in a highly dispersed state, supporting the validity of single-atom dispersion. Even at the highest loading of 2.0 wt%, the low density of approximately one Rh atom per 22 $BaTiO_3$ formula units indicates that Rh atoms are sufficiently separated from each other to prevent aggregation. The combination of XANES and EXAFS results demonstrated that Rh in BTO–RhSA exists as isolated Rh^{3+} single sites anchored to oxygen-containing surface groups without incorporation into the BTO lattice or formation of Rh-containing nanoparticles.

3.3. Investigation of piezoelectric properties

PFM measurements were performed to evaluate the piezoelectric responses of BTO and BTO–RhSA. The piezoelectric characteristics obtained are shown in Fig. 5. For both samples, typical amplitude-voltage butterfly loops were obtained. These results confirm that both BTO and BTO–RhSA exhibit clear polarization reversal behavior and are piezoelectrically active. Furthermore, no significant differences were observed in the PFM amplitude and phase responses between the BTO and BTO–RhSA samples. This indicates that RhSA does not affect the crystal symmetry or domain structure of BTO, thereby preserving its intrinsic piezoelectric properties. Thus, while the introduction of RhSA influences the surface reactivity, it does not alter the internal structure or the polarization characteristics of BTO. This result is consistent with the structural stability observed by XRD, SEM, and TEM, confirming that the Rh species did not diffuse into the BTO crystal but remained coordinatively bound to the surface.

3.4. Evaluation of piezocatalytic activity

Fig. 6 shows the time profiles of H_2O_2 formation over BTO and BTO–RhSA under ultrasonication. Both catalysts exhibited a continuous increase in H_2O_2 concentration, demonstrating that the piezoelectric polarization induced by mechanical stimulation effectively drove redox reactions at the catalyst surface. Table S1 summarizes the H_2O_2 concentrations obtained under O_2 and Ar saturation. Notably, no H_2O_2 was detected under Ar-saturation, where dissolved oxygen was eliminated from the system. This clearly indicates that the H_2O_2 formation pathway is the two-electron ORR rather than the two-electron water oxidation reaction. Therefore, in this reaction system, the following two half-reactions proceed:

Reduction half-reaction: $O_2 + 2H^+ + 2e^- \rightarrow H_2O_2$ (ORR)

Oxidation half-reaction: $(CH_3)_2CHOH \rightarrow (CH_3)_2CO + 2H^+ + 2e^-$ (isopropanol oxidation)

These results are consistent with prior reports on BTO-based piezocatalysts, where H_2O_2 generation proceeds *via* piezoelectrically induced charge separation followed by the ORR.[48] Furthermore, no H_2O_2 production was observed in the absence of ultrasonic vibration for both samples, confirming that the reaction is exclusively driven by the piezoelectric effect and not by thermal or photocatalytic processes. A comparison of the catalytic performance revealed that BTO–RhSA exhibited higher H_2O_2 generation than pristine BTO did. The H_2O_2 concentration generated by BTO–RhSA was approximately 1.5 times that generated by pristine BTO. This enhancement is attributed to the presence of RhSA on the BTO surface. The negligible

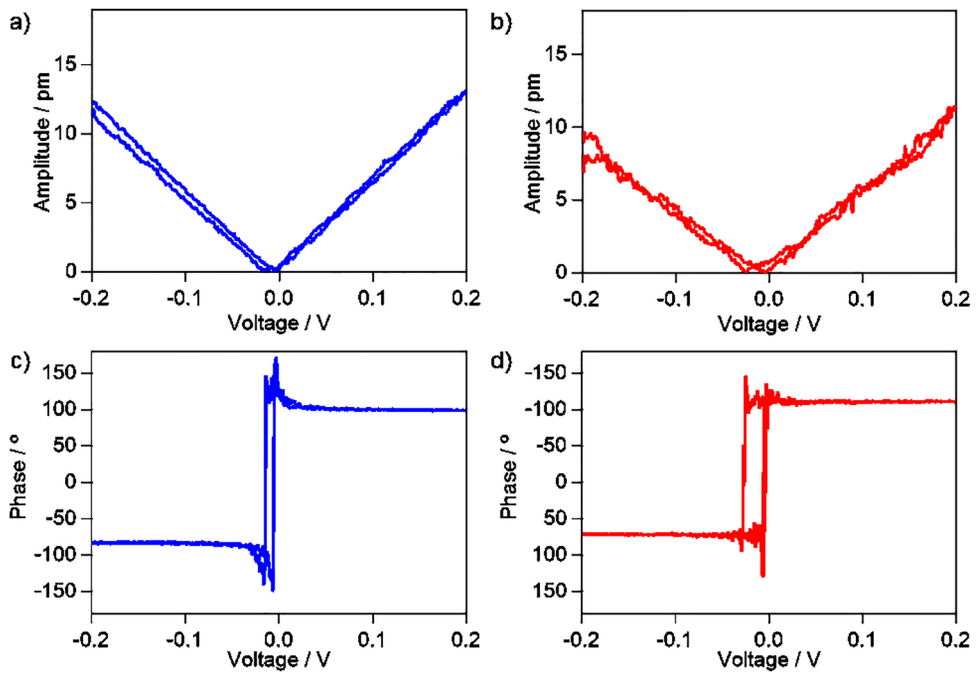

Fig. 5 (a) and (b) Piezoresponse amplitude butterfly curves and (c) and (d) phase hysteresis loops of (a) and (c) the pristine BTO and (b) and (d) BTO–RhSA.

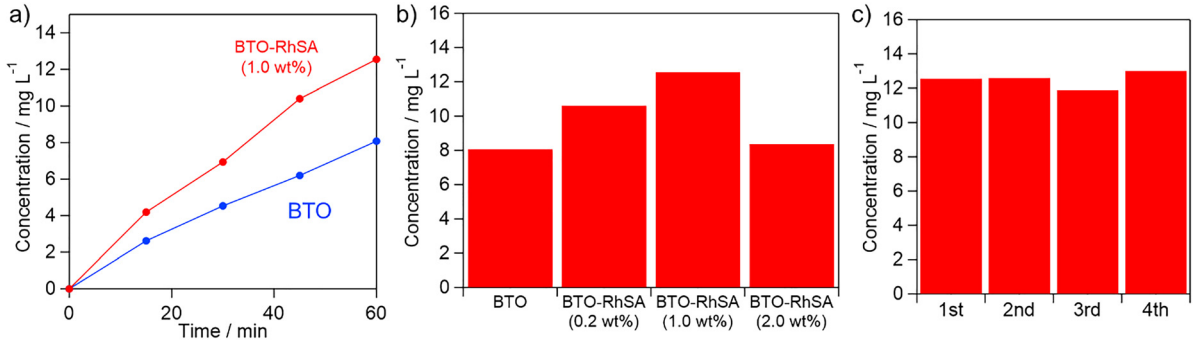

Fig. 6 (a) Time profiles of H_2O_2 production using the pristine BTO and BTO–RhSA. (b) H_2O_2 concentration produced during one-hour reactions using the pristine BTO and BTO–RhSA with different RhSA loadings. (c) H_2O_2 concentration produced during one-hour reactions using the BTO–RhSA (1 wt%) in repeated experiments.

H_2O_2 production upon ultrasonic treatment of a $RhCl_3$-containing solution further verified that the catalytic activity enhancement originated from the surface-anchored RhSA sites (Table S1). As shown above, BTO and BTO–RhSA exhibited similar morphologies and crystal structures, and only negligible differences existed in their piezoelectric polarizations. Therefore, the higher piezocatalytic activity of BTO–RhSA is attributed to the promotion of surface catalytic reactions rather than changes in intrinsic piezoelectric properties. The influence of the RhSA loading amount was investigated using BTO–RhSA samples with varying Rh contents (Fig. 6b). The catalytic activity increased with RhSA loading up to 1 wt%, beyond which the activity declined. In the low loading region (0.2 to 1.0 wt%), the number of surface Rh active sites increases with increasing Rh loading. RhSA sites are expected to function as active sites that promote surface reactions by utilizing charges generated by piezoelectric polarization. Therefore, an increase in Rh loading directly corresponds to an increase in the number of enhanced active sites. On the other hand, in the excessive loading region (above 1.0 wt%), a decrease in activity was observed. This activity decline is primarily attributed to the promotion of charge recombination. In piezocatalytic reactions, positive and negative charges generated by mechanical stimulation recombine and are deactivated if they are not consumed by appropriate surface reactions. Densely loaded Rh species may function as charge trapping sites, capturing both positive and negative charges and thereby facilitating their recombination. Although RhSA induces both the promotion of surface reactions and charge recombination regardless of the loading amount, the relative contribution of these two competing effects differs depending on the loading level. At low loadings, the promotion of surface reactions is the dominant factor because the influence of charge recombination is relatively minor, resulting in an overall enhancement in catalytic activity. Similar volcano-type trends have previously been reported for single-atom noble metal loading on oxide supports, where the optimal loading balances atomic dispersion and accessible reaction sites.[38,49] Thus, 1 wt% is identified as the optimal RhSA loading for piezocatalytic H_2O_2 production in this study. The durability of the optimized BTO–RhSA (1 wt%) catalyst was evaluated over four consecutive piezocatalytic cycles of 1 h each (Fig. 6c). The H_2O_2 production remained nearly constant for all cycles, demonstrating the excellent stability of BTO–RhSA. ICP-OES analysis of the reaction solution after the durability test revealed no detectable Rh species (below the detection limit of 0.01 ppm). Thus, no Rh species were dissolved in the solution after the durability test. Thus, RhSA is strongly fixed on the BTO surface and is resistant to metal leaching or atom migration owing to the strong metal–oxygen coordination. We compared the H_2O_2 production performance of BTO–RhSA with previously reported piezocatalysts (Table S2). Although the catalytic activity achieved in this study does not represent the highest value reported to date, the present catalyst exhibits performance that is fully comparable to those of state-of-the-art piezocatalysts reported in the literature. Overall, these findings establish that surface-anchored RhSA sites enhance the piezocatalytic H_2O_2 production efficiency of BTO, primarily by facilitating interfacial charge utilization and promoting reaction kinetics.

3.5. Identification of enhanced activity for BTO–RhSA

To elucidate the origin of the enhanced piezocatalytic activity of RhSA, the ORR abilities of BTO and BTO–RhSA were examined using LSV. As shown in Fig. 7a, both samples exhibited cathodic current densities below 0.3 V *vs.* RHE. Notably, BTO–RhSA displayed a current density similar to that of pristine BTO, indicating that the introduction of RhSA sites does not enhance the ORR activity of the BTO. This observation contrasts with the previous report in which Rh single atoms supported on TiO_2 promoted oxygen reduction kinetics.[38] The lack of ORR enhancement in BTO–RhSA suggests that the role of RhSA depends on the nature of the support, and that RhSA did not facilitate electron transfer to O_2 at the BTO interface. These findings clearly indicate that the activity enhancement by RhSA did not originate from the promotion of ORR. Next, we evaluated the oxidation ability of the catalysts using a piezoelectrochemical system. Chronoamperometric measurements were conducted at a constant potential of 1.0 V *vs.* RHE, during which periodic ultrasonic irradiation was applied to activate the piezoelectric effect (Fig. 7b). For both BTO and BTO–RhSA, ultrasonic excitation induced an increase in the current density, confirming that the oxidation of isopropanol sacrificial reagent was accelerated by piezoelectrically generated charges. Importantly, the magnitude of the current response was

greater for BTO–RhSA, and the current increase by ultrasonic stimulation was more pronounced than that of pristine BTO. These results clearly demonstrate that RhSA loading enhances the oxidation reaction. Besides, the (piezo)electrochemical measurements revealed that the primary reason for the enhanced piezocatalytic activity of BTO–RhSA is the promotion of the oxidation reaction rather than the reduction reaction.

3.6. Mechanism of activity enhancement by RhSA

Although the reaction mechanism of piezocatalysis remains under discussion, it is generally believed that the negative charges generated by mechanical stimulation drive reduction reactions, whereas positive charges drive oxidation reactions.[50] In the reaction system of this study, the reduction reaction involved the generation of H_2O_2 through the reduction of O_2, whereas the oxidation reaction involved the oxidation of isopropanol. If either reaction does not proceed sufficiently, charge quenching occurs more readily, resulting in decreased overall activity. Therefore, accelerating the rate-limiting reaction is key to achieving high activity. The results of (piezo)electrochemical measurements revealed that RhSA on BTO selectively promoted the oxidation reaction in piezocatalysis without contributing to the reduction reaction. Furthermore, PFM measurements indicated that the piezoelectric properties of BTO and BTO–RhSA were similar (Fig. 5), suggesting that the enhanced activity due to RhSA introduction was not attributable to the increased piezoelectric voltage. Moreover, as RhSA alone exhibited no piezocatalytic activity, it is considered that RhSA promotes the oxidation reaction by effectively utilizing the positive charge generated in the piezocatalytic reaction on BTO.

One possible mechanism for promotion of the oxidation reaction by RhSA involves the positive charges generated on the BTO surface converting trivalent RhSA to a higher oxidation state RhSA, which then oxidizes isopropanol. The highly oxidized RhSA species are expected to be extremely unstable, promoting isopropanol oxidation rapidly. This mechanism is similar to the photocatalytic oxidation reaction of photoexcited, highly oxidized Rh species reported for TiO_2 photocatalysts modified with RhSA.[38] In particular, highly oxidized RhSA exhibits greater reactivity towards alcohols than towards other substrates in photocatalysis.[39] In this piezocatalytic reaction system, it is also likely that similar highly oxidized RhSA species promote the oxidation of isopropanol.[37,39,51] The BTO–RhSA exhibited a higher H_2O_2 production activity than pristine BTO even in the absence of isopropanol (Table S1). However, the activity enhancement induced by RhSA was more limited compared with the case in the presence of isopropanol. The results indicate that RhSA promotes the oxidation of isopropanol more efficiently than that of water. These highly oxidized Rh species have short lifetimes, making their direct detection under the reaction conditions difficult. Other mechanisms are conceivable, and detailed clarification of the mechanisms is a future task. Previously reported single-atom piezocatalysts primarily employed methods to enhance their activity by introducing single-atom species into the bulk lattice.[40–42] In contrast, this study successfully introduced single atoms exclusively onto the catalyst surface for the first time, selectively enhancing the oxidation reaction in piezocatalytic reactions. This unique functionality, which is not observed in other cocatalysts, is expected to offer a new design strategy that broadens the potential applications of piezocatalysis.

4. Conclusion

We successfully synthesized BTO nanoparticles modified with atomically dispersed RhSA for piezocatalytic H_2O_2 production. Structural and morphological analyses confirmed that RhSA exists exclusively as isolated Rh^{3+} sites anchored on the BTO surface, with no formation of metallic clusters or lattice doping. The intrinsic crystal structure and piezoelectric polarization of BTO did not change after RhSA loading. The BTO–RhSA catalyst exhibited superior piezocatalytic activity for H_2O_2 generation *via* the two-electron oxygen reduction pathway, achieving optimal performance at 1 wt% RhSA loading with excellent

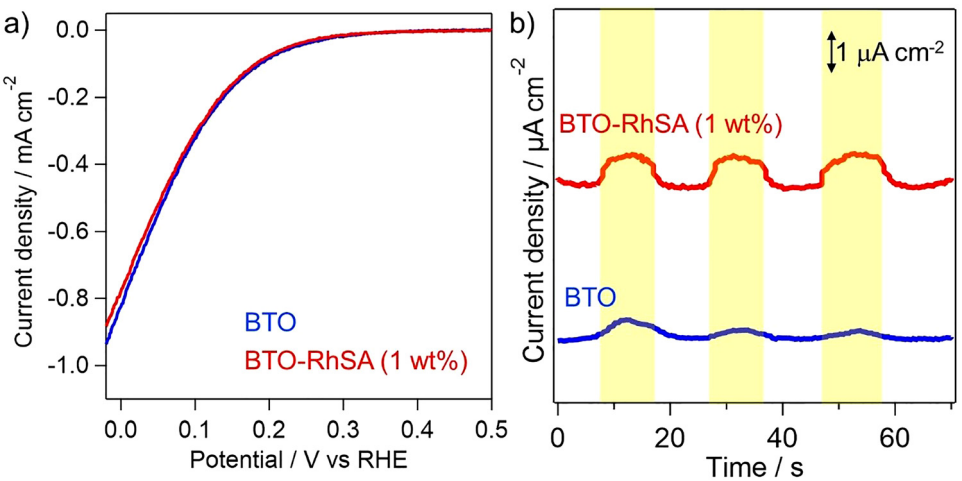

Fig. 7 (a) LSV curves of the pristine BTO and BTO–RhSA (1 wt%) for ORR. (b) Transient piezoelectric current responses of the pristine BTO and BTO–RhSA (1 wt%) recorded at an applied potential of 1.0 V *vs.* RHE; the yellow shaded regions indicate periods of ultrasonic irradiation.

durability. Electrochemical and piezoelectrochemical investigations revealed the unique role of the surface RhSA. The RhSA on BTO did not enhance the kinetics of the ORR. Instead, the activity enhancement was attributed to the promotion of the isopropanol oxidation reaction by the RhSA, likely involving highly oxidized Rh species. The efficient consumption of positive charges suppresses charge recombination, thereby facilitating the overall piezocatalytic reactions. This study highlights the potential of surface-anchored single atoms to modulate specific reactions in piezocatalysis, offering a distinct design strategy for developing advanced materials.

Conflicts of interest

There are no conflicts of interest to declare.

Data availability

All data can be found in the main article or the supplementary information (SI). Supplementary information on samples with different loading amounts, reaction results under control conditions, and comparisons with previously reported catalysts are presented. See DOI: https://doi.org/10.1039/d5cp04993h.

Acknowledgements

Funding: part of this study was conducted at the Multi-Quantum Beam High Voltage Electron Microscope Laboratory at Hokkaido University, supported by the Advanced Research Infrastructure for Materials (ARIM) Project, funded by the Ministry of Education, Culture, Sports, Science and Technology (MEXT), Japan (JPMXP1224HK0053). This study was supported by JSPS Kakenhi (22K05295).

References

1 N. Meng, W. Liu, R. Y. Jiang, Y. Zhang, S. Dunn, J. Y. Wu and H. X. Yan, *Prog. Mater. Sci.*, 2023, **138**, 101161.
2 H. L. Hou, X. K. Zeng and X. W. Zhang, *Angew. Chem., Int. Ed.*, 2020, **59**, 17356.
3 C. Kim, S. O. Park, S. K. Kwak, Z. H. Xia, G. Kim and L. M. Dai, *Nat. Commun.*, 2023, **14**, 5822.
4 H. Kominami, K. Kamitani and A. Tanaka, *Chem. Commun.*, 2024, **60**, 7017.
5 H. X. Cao, G. Chen, Y. Yan and D. Wang, *ChemSusChem*, 2025, **18**, e202401100.
6 S. C. Tu, Y. X. Guo, Y. H. Zhang, C. Hu, T. R. Zhang, T. O. Y. Ma and H. W. Huang, *Adv. Funct. Mater.*, 2020, **30**, 2005158.
7 X. F. Zhou, B. Shen, A. Lyubartsev, J. W. Zhai and N. Hedin, *Nano Energy*, 2022, **96**, 107141.
8 L. F. Zhao, M. Y. Xu, S. J. Yang, Z. Y. Zhu, J. G. Qi and F. Q. Meng, *ACS Sustainable Chem. Eng.*, 2025, **13**, 8853.
9 Y. Zhang, H. Khanbareh, S. Dunn, C. R. Bowen, H. Y. Gong, N. P. H. Duy and P. T. T. Phuong, *Adv. Sci.*, 2022, **9**, 2105248.
10 K. S. Hong, H. F. Xu, H. Konishi and X. C. Li, *J. Phys. Chem. Lett.*, 2010, **1**, 997.
11 H. L. You, Z. Wu, L. H. Zhang, Y. R. Ying, Y. Liu, L. F. Fei, X. X. Chen, Y. M. Jia, Y. J. Wang, F. F. Wang, S. Ju, J. L. Qiao, C. H. Lam and H. T. Huang, *Angew. Chem., Int. Ed.*, 2019, **58**, 11779.
12 D. F. Yu, Z. H. Liu, J. M. Zhang, S. Li, Z. C. Zhao, L. F. Zhu, W. S. Liu, Y. H. Lin, H. Liu and Z. T. Zhang, *Nano Energy*, 2019, **58**, 695.
13 J. M. Wu, W. E. Chang, Y. T. Chang and C. K. Chang, *Adv. Mater.*, 2016, **28**, 3718.
14 F. J. Li, S. F. Guo, J. Shi and Q. An, *ChemPlusChem*, 2023, **88**, e202300324.
15 M. H. Wu, J. T. Lee, Y. J. Chung, M. Srinivaas and J. M. Wu, *Nano Energy*, 2017, **40**, 369.
16 X. Q. Dai, L. Chen, Z. Y. Li, X. J. Li, J. F. Wang, X. Hu, L. H. Zhao, Y. M. Jia, S. X. Sun, Y. Wu and Y. M. He, *J. Colloid Interface Sci.*, 2021, **603**, 220.
17 J. P. Ma, X. Xiong, D. Wu, Y. Wang, C. G. Ban, Y. J. Feng, J. Z. Meng, X. S. Gao, J. Y. Dai, G. Han, L. Y. Gan and X. Y. Zhou, *Adv. Mater.*, 2023, **35**, 2300027.
18 Y. M. Wang, H. C. Ma, J. J. Liu, Z. Zhang, Y. C. Yu and S. L. Zuo, *J. Colloid Interface Sci.*, 2023, **642**, 304.
19 M. X. Zhang, S. Y. Zhao, Z. C. Zhao, S. Li and F. Wang, *ACS Appl. Mater. Interfaces*, 2021, **13**, 10916.
20 X. C. Liu, M. W. Wang, Y. Li, X. X. Li, J. J. Zhang, S. Yang, J. Wu, L. H. Wang, J. L. Li and F. Li, *J. Colloid Interface Sci.*, 2025, **678**, 246.
21 Q. Tang, J. Wu, X. Z. Chen, R. Sanchis-Gual, A. Veciana, C. Franco, D. Kim, I. Surin, J. Pérez-Ramfrez, M. Mattera, A. Terzopoulou, N. Qin, M. Vukomanovic, B. J. Nelson, J. Puigmartf-Luis and S. Pan, *Nano Energy*, 2023, **108**, 108202.
22 C. Y. Wang, F. Chen, C. Hu, T. Y. Ma, Y. H. Zhang and H. W. Huang, *Chem. Eng. J.*, 2022, **431**, 133930.
23 Y. H. Cheng, J. Chen, P. F. Wang, W. Liu, H. A. Che, X. Gao, B. Liu and Y. H. Ao, *Appl. Catal., B*, 2022, **317**, 121793.
24 S. F. Jia, Y. P. Su, B. P. Zhang, Z. C. Zhao, S. Li, Y. F. Zhang, P. C. Li, M. Y. Xu and R. Ren, *Nanoscale*, 2019, **11**, 7690.
25 Y. Q. Zheng, Y. M. Jia, H. M. Li, Z. Wu and X. P. Dong, *J. Mater. Sci.*, 2020, **55**, 14787.
26 Y. X. Shi, L. L. Li, Z. Xu, F. Guo, Y. Li and W. L. Shi, *Appl. Surf. Sci.*, 2023, **616**, 156466.
27 W. X. Xu, K. Li, L. B. Shen, X. Y. Liu, Y. Chen, J. K. Feng, W. W. Zhao, L. L. Zhao, W. J. Zhou, W. J. Wang and J. H. Li, *ChemCatChem*, 2022, **14**, e202200312.
28 E. Z. Lin, J. Wu, N. Qin, B. W. Yuan and D. H. Bao, *Catal. Sci. Technol.*, 2018, **8**, 4788.
29 S. Li, Z. C. Zhao, D. F. Yu, J. Z. Zhao, Y. P. Su, Y. Liu, Y. H. Lin, W. S. Liu, H. Xu and Z. T. Zhang, *Nano Energy*, 2019, **66**, 104083.
30 S. Li, Z. C. Zhao, M. S. Liu, X. B. Liu, W. Huang, S. K. Sun, Y. H. Jiang, Y. Liu, J. M. Zhang and Z. T. Zhang, *Nano Energy*, 2022, **95**, 107031.
31 G. D. Yang, Q. Chen, W. J. Wang, S. J. Wu, B. J. Gao, Y. B. Xu, Z. Chen, S. X. Zhong, J. R. Chen and S. Bai, *ACS Appl. Mater. Interfaces*, 2021, **13**, 15305.

32 Y. J. Chen, S. F. Ji, C. Chen, Q. Peng, D. S. Wang and Y. D. Li, *Joule*, 2018, **2**, 1242.
33 A. Q. Wang, J. Li and T. Zhang, *Nat. Rev. Chem.*, 2018, **2**, 65.
34 Y. R. Li, Z. W. Wang, T. Xia, H. X. Ju, K. Zhang, R. Long, Q. Xu, C. M. Wang, L. Song, J. F. Zhu, J. Jiang and Y. J. Xiong, *Adv. Mater.*, 2016, **28**, 6959.
35 Y. Xia, M. Sayed, L. Y. Zhang, B. Cheng and J. G. Yu, *Chem. Catal.*, 2021, **1**, 1173.
36 S. Kitano, K. Hashimoto and H. Kominami, *Catal. Today*, 2011, **164**, 404.
37 S. Kitano, K. Hashimoto and H. Kominami, *Appl. Catal., B*, 2011, **101**, 206.
38 S. Kitano, N. Murakami, T. Ohno, Y. Mitani, Y. Nosaka, H. Asakura, K. Teramura, T. Tanaka, H. Tada, K. Hashimoto and H. Kominami, *J. Phys. Chem. C*, 2013, **117**, 11008.
39 S. Kitano, A. Tanaka, K. Hashimoto and H. Kominami, *Phys. Chem. Chem. Phys.*, 2014, **16**, 12554.
40 X. J. Shen, C. L. Pan, X. Z. Wei, J. Z. Liu, M. Y. Liu, G. Y. Liu and M. L. Pan, *ACS Nano*, 2025, **19**, 28257.
41 Y. T. Wang, H. Y. Lin, Y. C. Chen, Y. G. Lin and J. M. Wu, *Small Methods*, 2024, **8**, 2301287.
42 Q. J. Xu, L. L. Wang, X. L. Sheng, Y. X. Yang, C. H. Zhang, L. Y. Duan and H. Guo, *Appl. Catal., B*, 2023, **338**, 123058.
43 Q. Feng, Y. Ishikawa, Y. Makita and Y. Yamamoto, *J. Ceram. Soc. Jpn.*, 2010, **118**, 141.
44 S. Kitano, K. Hashimoto and H. Kominami, *Chem. Lett.*, 2010, **39**, 627.
45 J. Wu, N. Qin and D. H. Bao, *Nano Energy*, 2018, **45**, 44.
46 S. Kitano, M. Sadakiyo, K. Kato, M. Yamauchi, H. Asakura, T. Tanaka, K. Hashimoto and H. Kominami, *Appl. Catal., B*, 2017, **205**, 340.
47 S. Yan, Z. Z. Cao, Q. Liu, Y. F. Gao, H. Zhang and G. R. Li, *J. Alloys Compd.*, 2022, **923**, 166398.
48 K. Wang, M. Q. Zhang, D. G. Li, L. H. Liu, Z. P. Shao, X. Y. Li, H. Arandiyan and S. M. Liu, *Nano Energy*, 2022, **98**, 107251.
49 Z. N. Wu, I. Hwang, G. Cha, S. S. Qin, O. Tomanec, Z. Badura, S. Kment, R. Zboril and P. Schmuki, *Small*, 2022, **18**, 2104892.
50 Y. M. Lin, D. Mou, X. R. Pu, B. Li, L. M. Jiang and X. H. Zhu, *Mater. Today*, 2025, **86**, 414.
51 S. Kitano, A. Tanaka, K. Hashimoto and H. Kominami, *Appl. Catal., A*, 2016, **521**, 202.